A&A 409, 193–203 (2003)
DOI: 10.1051/0004-6361:20031076

Astronomy
&
Astrophysics

ISOCAM-CVF imaging of M 16[⋆]

J. S. Urquhart[1], Glenn J. White[1,2], G. L. Pilbratt[3], and C. V. M. Fridlund[3]

[1] Centre for Astrophysics and Planetary Science, School of Physical Sciences, University of Kent, Canterbury, CT2 7NR, UK
[2] Stockholm Observatory, Department of Astronomy, 106 91 Stockholm, Sweden
[3] ESA Astrophysics Missions Division, Research and Science Support Department, ESTEC, PO Box 299,
2200 AG Noordwijk, The Netherlands

Received 15 April 2003 / Accepted 2 July 2003

Abstract. We present ISOCAM observations (5–17 μm) of the HST M 16 field, including the striking elephant trunk structures. The spectroscopic data have been obtained using the ISOCAM-CVF low-resolution mode, having a spectral resolution of $\sim$40 ($\lambda/\Delta\lambda$) and a pixel size of 6″. The spectra show a combination of Unidentified Infrared Band (UIB) emission centred at 6.2, 7.7, 8.6, 11.3 and 16.4 μm, and atomic fine-structure lines of [ArII] 7.0 μm, [ArIII] 9.0 μm, [SIV] 10.5 μm, [NeII] 12.8 μm and [NeIII] 15.6 μm. The spectra were decomposed by fitting a combination of Lorentzian line profiles and a blackbody curve to the data to produce maps of the spatial distribution of the fine-structure and UIB emission features. These maps have been compared with VLA radio, 450 μm SCUBA maps, ^{12}CO ($J = 1{-}0$) maps, and broadband filters ISOCAM LW2 (5–8.5 μm) and LW3 (12–18 μm) observations. Decomposed spectral features have shown that the LW2 filter is dominated by UIB emission and the emission observed in the LW3 filter is a combination of Neon fine-structure lines and a steep continuum, with the continuum dominating. Using the photoionisation code CLOUDY we have produced theoretical values for the fine-structure ratio of [NeIII] 15.6 μm/[NeII] 12.8 μm, from which we have calculated the effective ionising flux impinging onto the tips of the pillars to be $\sim 1{-}3 \times 10^{10}$ photons cm^{-2} s^{-1}, consistent with estimates made from VLA observations.

Key words. ISM: HII regions – ISM: lines and bands – infrared: ISM – ISM: individual object: Eagle Nebula

1. Introduction

The “Eagle Nebula” in M 16 is a prominent HII region lying a distance of $\sim$2 kpc (Hillenbrand et al. 1993; hereafter Hi93) from the Earth. The region contains three “elephant trunk” or “molecular pillars” structures protruding into the surrounding HII region from the parent molecular cloud, where Π_1, Π_2 and Π_3 label the pillars running from north-west to south-east (following the notation introduced by Pilbratt et al. 1998; hereafter Pi98; and used by White et al. 1999; hereafter Wh99), see Fig. 1.

The HII region is excited by a recently formed stellar cluster (NGC 6611) that contains several O5 stars located $\sim$2 pc to the north-west (Hi93). These O type stars are the principal source of ionising radiation in the nebula, emitting a combined photon flux of $\sim 2 \times 10^{50}$ photons s^{-1} (Hester et al. 1996; hereafter He96). The ionising cluster appears to be in a plane of sky that lies between the Π_1 and Π_2–Π_3, with the nearside tip of Π_1 being fully illuminated and therefore presumably in the background, while the remaining two are optically opaque with only the tips illuminated, and therefore probably in the foreground.

The pillar structures are thought to have resulted from the interaction between the UV radiation from the young massive stars in the cluster and the molecular cloud out of which they formed (He96, Wh99). These structures are generally assumed to have been produced when the expanding ionisation front, driven by the massive stars, was impeded by high density regions present in the inhomogeneous molecular cloud (which are now in the tips of the pillars), while the lower density material between the pillars was photoionised by the Far–UV (FUV) radiation field, and driven off the surface by radiation pressure and strong stellar winds. This process produces the cometary morphology, with the high density material forming the head, and the tail being formed from low density material shielded from the ionising radiation, and the low-density gas swept directly away from the ionising source.

It is widely believed that the O5 stars ionise the surface of the pillars, creating a layer of hot ionised gas surrounding the tips of the pillars. This surrounding layer of high pressure ionised gas, seen in the Hα images taken by the Hubble Space Telescope (HST; He96) and in the extended free-free radio emission seen in images taken by the VLA (Wh99), is thought to compress the underlying dense molecular material at the tips of the pillars, driving shock fronts into the molecular gas as

---

Send offprint requests to: J. S. Urquhart,
e-mail: `jsu@star.ukc.ac.uk`

[⋆] Based on observations with ISO, an ESA project with instruments funded by ESA Member States (especially the PI countries: France, Germany, The Netherlands and the UK) and with the participation of ISAS and NASA.

the ionised gas expands into the low-density HII region, possibly triggering a next generation of star formation though the process known as Radiatively Driven Implosion (RDI; Bertoldi 1989; Lefloch & Lazareff 1994).

The interface between the tips of the trunks and the surrounding HII region have been investigated by He96 who reported the presence of 73 small protrusions on, or near, the surface of the tips of the pillars, denoting them as Evaporating Gaseous Globules (EGGs). He96 proposed that these protrusions were the over-dense condensations of molecular material present in the pillars prematurely uncovered as the ionisation front, driven by NGC 6611, propagates through the pillars and therefore these EGGs are potential sites for low-mass stars to hatch. Near-Infrared (NIR) observations of the EGGs near the Eagle nebula (McCaughrean 1997; McCaughrean & Andersen 2002) concluding that the majority contained no embedded NIR sources, but that a small proportion (~15%) did show evidence of embedded sources, possibly indicating the presence of a low-mass star or brown dwarf. Pi98 observed the Pillars in the mid-Infrared (MIR) using two ISOCAM (Cesarsky et al. 1996a) broadband filters LW2 (5–8.5 μm) and LW3 (12–18 μm) on the Infrared Space Observatory (ISO; Kessler et al. 1996) in an attempt to correlate MIR sources with EGGs seen in the HST images, but due to poor angular resolution and sensitivity this was not conclusive.

More recently deep NIR observations (Sugitani et al. 2002; Thompson et al. 2002) of the pillars have revealed numerous Young Stellar Objects (YSOs) and provided evidence of massive star formation, particularly towards the tips of Π_1 and Π_2. This is consistent with recent star formation triggered by the interaction of the FUV radiation on the tips of the pillars, possibly by the RDI mechanism.

Submillimetre observations of the pillars have revealed the presence of cold dense cores ~10–20 K, at the heads of each pillar, with masses of $\Pi_1 \sim 60\ M_{\odot}$, $\Pi_2 \sim 31\ M_{\odot}$ and $\Pi_3 \sim 11\ M_{\odot}$ leading Wh99 to suggest that these dense cores, that form the heads of the cometary shaped pillars, are at an early stage of protostellar formation. Pound (1998) mapped the molecular gas in and around the pillars in ^{12}CO (J = 1–0), ^{13}CO (J = 1–0) and ^{12}C^{18}O (J = 1–0) emission with a resolution of 10″, which revealed the dramatic effect the nearby O stars are having on the pillars reporting steep velocity gradients up to 20 km s^{-1} in the molecular gas. Fukuda et al. (2002; hereafter FHS02) have made observations of the heads of Π_1 and Π_2 in the ^{13}CO (J = 1–0) and the C^{18}O (J = 1–0) lines, reporting a steep intensity gradient in the ^{13}CO (J = 1–0) emission on the tips of the pillars closest to the ionising cluster, lending support to the theory that the structure of the pillars is a direct result of their interaction with the radiation and the stellar winds of the ionising stars. Three local peaks of ^{13}CO (J = 1–0) emission around the heads of both pillars have also been reported (FHS02), with the most luminous in both cases being located near the tips, as well as several dense cores detected in C^{18}O (J = 1–0) emission.

In this paper we use ISOCAM Circular Variable Filter (CVF) observations to investigate the spatial distribution of atomic and molecular gas across the M 16 field, comparing these distributions with observations made at different wavelengths. In Sect. 2 we describe the details of the observations and the methods employed in the data reduction. In Sect. 3 we present brightness distribution maps produced by decomposing the emission features identified in the CVF data and present modelling of the fine-structure lines. We present our conclusions in Sect. 4.

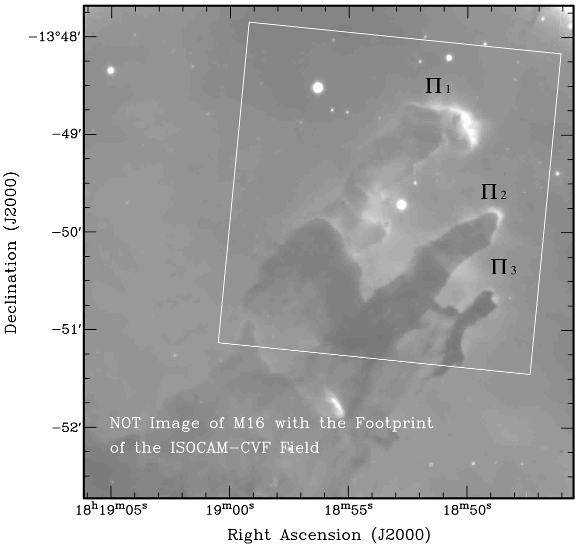

Fig. 1. Hα image of the Eagle nebula taken on the 1st January 2001 with the Nordic Optical Telescope (NOT) using the ALFOSC instrument, La Palma. The footprint of the ISOCAM-CVF field is outlined by the white square. The three pillars can clearly be seen in this image running north-west to south-east and will be referred to as Π_1, Π_2 and Π_3 respectively.

2. Observations and data reduction

2.1. Observations

The data presented were observed using ISOCAM on the ISO on the 19th October 1997. The observation was centred on RA = $18^{\mathrm{h}}18^{\mathrm{m}}53\overset{\mathrm{s}}{.}20$, Dec = $-13^{\circ}49'39\overset{''}{.}0$ (J2000), with an integration time of 4840 s. Imaging spectroscopy was obtained using CVF in its low-spectral resolution mode, sampling between 5–17 μm with spectral resolution between 35–50 and a pixel size of 6″ (at the distance to the M 16 corresponds to a linear resolution ~2.1×10^{17} cm, or ~14 000 AU). The 32×32 pixel detector array of ISOCAM had a total field of view 3′ × 3′ (see Fig. 1 for CVF field-of-view outlined by a white square).

2.2. Data reduction and extraction of spectral features

The data reduction was performed using the CAM Interactive Analysis software package (CIA; Ott et al. 1997)[1] using the standard reduction techniques described in Starck et al. (1999). The raw data were corrected for dark current and flatfields using the ISOCAM calibration libraries. The "Multi-resolution Median Transform" method was used to eliminate cosmic ray hits from the data. Memory effects, due to the long time

---

[1] CIA is a joint development by ESA Astrophysics Division and the ISOCAM Consortium led by the ISOCAM PI, C. Cesarsky.

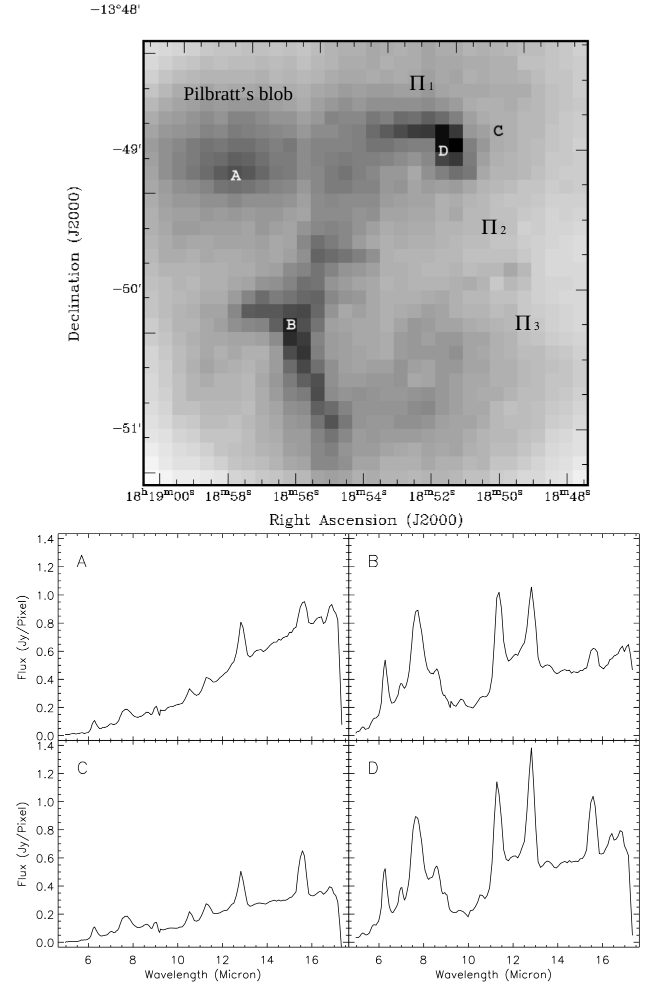

Fig. 2. Left: Broadband infrared image of the Eagle nebula taken by ISOCAM over the 5.1–17 μm wavelength range. The brightest regions are the head of Π_1 (labelled D) and the ridge between the base of Π_1 and Π_2 (labelled B), with the trunk like structure of Π_1 weakly visible and Π_2 and Π_3 visible only as a diffuse region of emission. Another feature to note is a region of bright emission to the NE of Π_1 (labelled A, and referred to in this paper as "Pilbratt's blob") comparable in strength to the emission from the head of Π_1 and the ridge. This region of bright was detected by Pi98 in their LW3 image, but not detected in the shorter wavelength LW2 image. In the CVF mode a complete spectrum is recorded for each pixel over the ~5–17 μm range. Right: CVF spectra of four regions of particular interest. Clockwise, Pilbratt's blob (A), the ridge connecting Π_1 and Π_2 (B), ionised region between tip of Π_1 and ionising source and tip of Π_1 (C), and finally the bright emission detected at the tip of Π_1 (D).

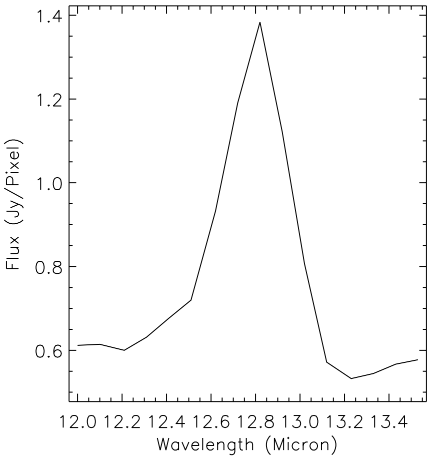

Fig. 3. The image above is a closeup of the blended UIB 12.7 μm and the [NeII] 12.8 μm lines taken from the location labelled D in Fig. 2. This image clearly shows the blended feature centred at 12.8 μm, as well as a slight shoulder located on the blue side of the blended feature, due to weak UIB 12.7 μm emission.

constant of the detector array, were corrected for using the "IAS model" (cf. Abergel et al. 1996).

In Fig. 2 we present a broadband (5–17 μm) infrared image of the three pillars along with four examples of the CVF spectra obtained from locations across the field as indicated in Fig. 2. The first and second pillar, Π_1 and Π_2, as well as the ridge connecting the base of the same two pillars can be seen clearly. Additionally, a bright diffuse region can be seen in the north-east of the head of Π_1, previously reported by Pi98 in their LW3 image; hereafter referred to as "Pilbratt's blob". The spectra have been chosen to correspond to areas of particular interest across the field, namely the three brightest regions and the region of ionised gas in front of Π_1.

The appearance of the 4 spectra vary quite dramatically across the field. Pilbratt's blob (A) displays a steep continuum, with very weak or little emission from the UIBs and with only a few, weak fine-structure lines. The head of Π_1 (D) and the connecting ridge (B) have similar spectra, both showing the same shape continuum and the presence of an absorption feature between 9.0–10 μm, but Π_1 shows stronger emission features at longer wavelengths regions ($\lambda \geq 10$ μm). The region of weak emission in between the ionising source and Π_1 (C) shows a weak continuum and two strong emission lines in the 12–16 μm wavelength region.

The emission features within the CVF wavelength coverage have been extensively studied in a wide range of astrophysical environments using ISO, and a full discussion of individual emission feature identification and characteristics are available (cf. Verstraete et al. 1996). As can be seen from Fig. 3, the spectrum over the wavelength region is rich and complex, containing broadband features, atomic fine-structure lines and hydrogen rotational line emission. As well as the emission features there is a continuum component which dominates at longer wavelengths (>10 μm), widely attributed to the presence of Very Small Grains (VSGs), warm dust ~10 nm in radius in thermal equilibrium with the radiation field (Desert et al. 1990).

The most prominent of these lines were identified to be associated with the UIBs (see Sect. 3) centred at 6.2, 7.7, 8.6, 11.3, 16.4 μm (Boulanger et al. 1998; hereafter Bo98; Moutou et al. 2000), and [ArII] 7.0 μm, [ArIII] 9.0 μm, [SIV] 10.5 μm and [NeIII] 15.6 μm hydrogen rotational line $H_2S(0)$ at 17.1 μm. There is some ambiguity in the identification of the strong emission feature centred at 12.8 μm due to the presence of two possible emission features in close proximity and the low-spectral resolution of the instrument. The 12.8 μm feature is the result of a blending of a UIB centred at 12.7 μm and [NeII] 12.8 μm, see Fig. 3. The effect of the blending can be seen as a slight shoulder on the blue side of the

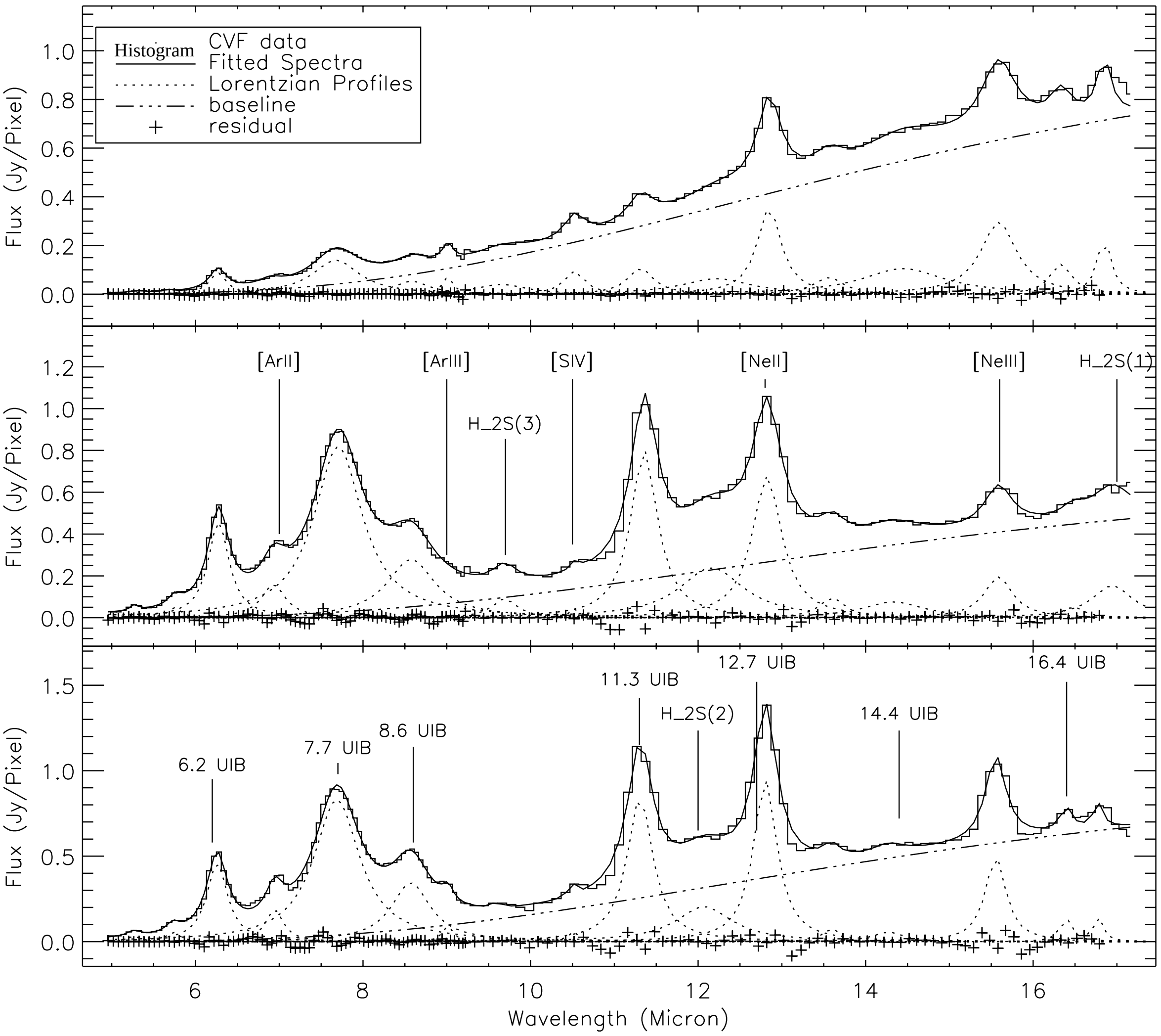

Fig. 4. Spectra taken from 6″ × 6″ pixel field-of-view centred at the locations denoted by the labels A (*top panel*), B (*centre panel*), and D (*bottom panel*) in Fig. 2.

feature. As previously noted in regions of low level star formation (Bo98) the 12.7 μm UIB feature is weaker than that of the 11.3 μm feature, but in our spectra the opposite is seen, which would suggest that most of the observed flux is due to [NeII] 12.8 μm ionic emission as previously reported by Le Floc'h et al. (2001).

In addition to the features already mentioned a number of weaker features can also be seen in the spectra which have been identified as, UIBs centred at 5.3, 5.7, 13.3 and 14.4 μm (Laurent et al. 2000) and hydrogen rotational lines at 9.7 and 12.0 μm. As well as the emission features, a region of absorption can be seen in the 9–10 μm wavelength band. This absorption region is generally assumed to be due to absorption by small dust grains and silicates.

The CVF data have been decomposed by fitting a combination of 17 Lorentzian profiles, one for each of the spectral emission features identified as suggested by Bo98 and supported by work presented by Verstraete et al. (2001). A blackbody curve (T = 200 K) was also introduced to account for the contribution VSGs make to the underlying continuum following the method described by Laurent et al. (2000). The reduced data was analysed using the Interactive Data Language (IDL) software package. We developed a multiple Lorentzian baseline fitting routine to separate out the individual emission features, by simultaneously fitting the blackbody curve (representing the continuum) in addition to a Lorentzian profile to each of the individual lines. This method produced an excellent fit to the data, some examples of the results are presented in Fig. 4. The fitting parameters of the Lorentzian profiles were then used to estimate the integrated flux for each emission feature, in each pixel. The integrated flux was then used to produce maps of the spatial and intensity distribution of each feature over the entire field (see Fig. 5).

Many of the emission features proved to be too weak to produce suitable maps of their spatial brightness distribution. We therefore concentrated on the nine most prominent features for the remainder of this paper, fitting the blended features of the 12.7 μm UIB and the [NeII] 12.8 μm line with a single Lorentzian profile centred at ~12.8 μm. Using the method previously described nine maps have been produce of the spatial distribution of four of the UIB features at 6.2, 7.7, 8.6 and 11.3 μm, and the five fine-structure ionic

Table 1. Summary of the Lorentzian coefficients and integrated flux resulting from fitting Lorentzian profiles to a pixel (Labelled D) on the head of Π_1.

Emission Line λ (μm)	Peak Wavelength λ (μm)	Peak flux (Jy)	*FWHM* ($\delta\lambda$)	Intensity (W m^{-2})
UIB 6.2	6.26	4.4×10^{-1}	2.9×10^{-1}	2.0×10^{-27}
[ArII] 7.0	6.95	1.7×10^{-1}	2.2×10^{-1}	6.0×10^{-28}
UIB 7.7	7.69	8.1×10^{-1}	6.5×10^{-1}	8.25×10^{-27}
UIB 8.6	8.57	3.4×10^{-1}	5.7×10^{-1}	3.05×10^{-27}
[ArIII] 9.0	9.01	9.0×10^{-2}	1.6×10^{-1}	2.5×10^{-28}
UIB 11.3	11.30	8.6×10^{-1}	3.9×10^{-1}	5.25×10^{-27}
UIB & [NeII] 12.8	12.81	10.1×10^{-1}	3.7×10^{-1}	5.85×10^{-27}
[NeIII] 15.6	15.56	6.6×10^{-1}	4.5×10^{-1}	4.65×10^{-27}

transitions of [ArII] 7.0 μm, [ArIII] 9.0 μm, [SIV] 10.5 μm, [NeII] 12.8 μm and [NeIII] 15.6 μm. These observed emission line and their corresponding fluxes are summarised in Table 1.

3. ISOCAM-CVF images

3.1. Analysis of images of spectral features

The difference between the UIB and fine-structure line emission can be clearly seen from the spatial distribution maps presented in Fig. 5. The two different types of observed emission features seen in our spectra are produced in different regions. The UIB emission is produced by molecules that are transiently heated to high temperatures each time they absorb a UV photon (Lèger & Puget 1984) present in the stellar radiation field of a massive star, and found in Photodissociation Regions (PDRs) surrounding HII regions, and as such are considered good tracers of star formation. The ionic emission lines do not originate inside the PDRs due to extremely high extinction, but can be produced on their surfaces and in the material that has been photo-evaporated off the surface, into the surrounding HII region (Hester 1991).

The maps produced of the UIB features are very well correlated with each other, all showing a very bright rim of emission around the head of Π_1 and along the ridge connecting Π_1 and Π_2. The shape of the second pillar is just weakly visible and not very well resolved. The two regions of strong emission are considerably brighter than anything else in the field by up to a factor of 3. This was first noted by Pi98 in observations made of the same field using the two ISOCAM broadband filters, LW2 and LW3. Little, or no, UIB emission is observed externally of the pillars, possibly indicating the destruction of the emitting molecules by the hard radiation field, or non-efficiency of the excitation mechanism (Onaka et al. 2000). The lack of emission outside of the pillars leads us to suggest that the contribution of 12.7 μm UIB emission to the blended feature centred at 12.8 μm is negligible.

Maps of the five fine-structure lines identified in the CVF spectra are presented in Fig. 5. The maps produced from the ionic transition lines are very different with each line having a different distribution. Although both Argon lines are affected by poor spectral resolution (being only partially resolved) and are affected by the presence of the silicate absorption on the red side of [ArIII] 9.0 μm, leading to a degree of contamination in their maps compared to the Neon maps. The [ArII] 7.0 μm and the [NeII] 12.8 μm images correlate well with those of the UIBs, but the emission from [ArIII] 9.0 μm and the [NeIII] 15.6 μm is much more diffuse.

The higher ionisation states of [ArIII] 9.0 μm and [NeIII] 15.6 μm have very different distributions, both appearing to show diffuse emission outside of, and between the pillars. The strongest emission from [ArIII] 9.0 μm is located in a pocket on the surface of Π_1 that correlates well with the VLA radio map, and has a bright region just above (in the direction of the ionising source) the ridge connecting the base of Π_1 & Π_2. [NeIII] 15.6 μm displays a bright region around the tip of Π_1, which coincides with the bright region seen in the [NeII] 12.8 μm map, but peaks closer to the ionising stars. Three small dark regions, denoting very low levels of emission, can be seen in both the [ArIII] 9.0 μm and the [NeIII] 15.6 μm. These dark regions coincide with the heads of the three pillars corresponding to the three cores seen in the 450 μm SCUBA image, the result of shielding by dense material around the tips of the pillars.

The difference in the emission maps arising from different atomic ionisation level of the two elements can be understood by considering the ionisation potential of each ionic line. The ionisation potential of the higher ionisation state of [ArIII] 9.0 μm and [NeIII] 15.6 μm are considerably larger than that of the [NeII] 12.8 μm and the [ArII] 7.0 μm. We would therefore expect the levels with the higher ionisation potential to peak closer to the ionisation source where the FUV radiation field is stronger, which is observed.

3.2. Comparison with broadband LW2 and LW3 images

From a comparison of the spatial distribution maps produced of the various UIB features, the 7.7 μm UIB feature has the best spatial definition. It is also the strongest of the UIB emission features (optimal signal to noise), and is relatively unaffected by the silicate absorption at 9.7 μm compared with the 11.3 and the 8.6 μm UIB emission. We have therefore used this

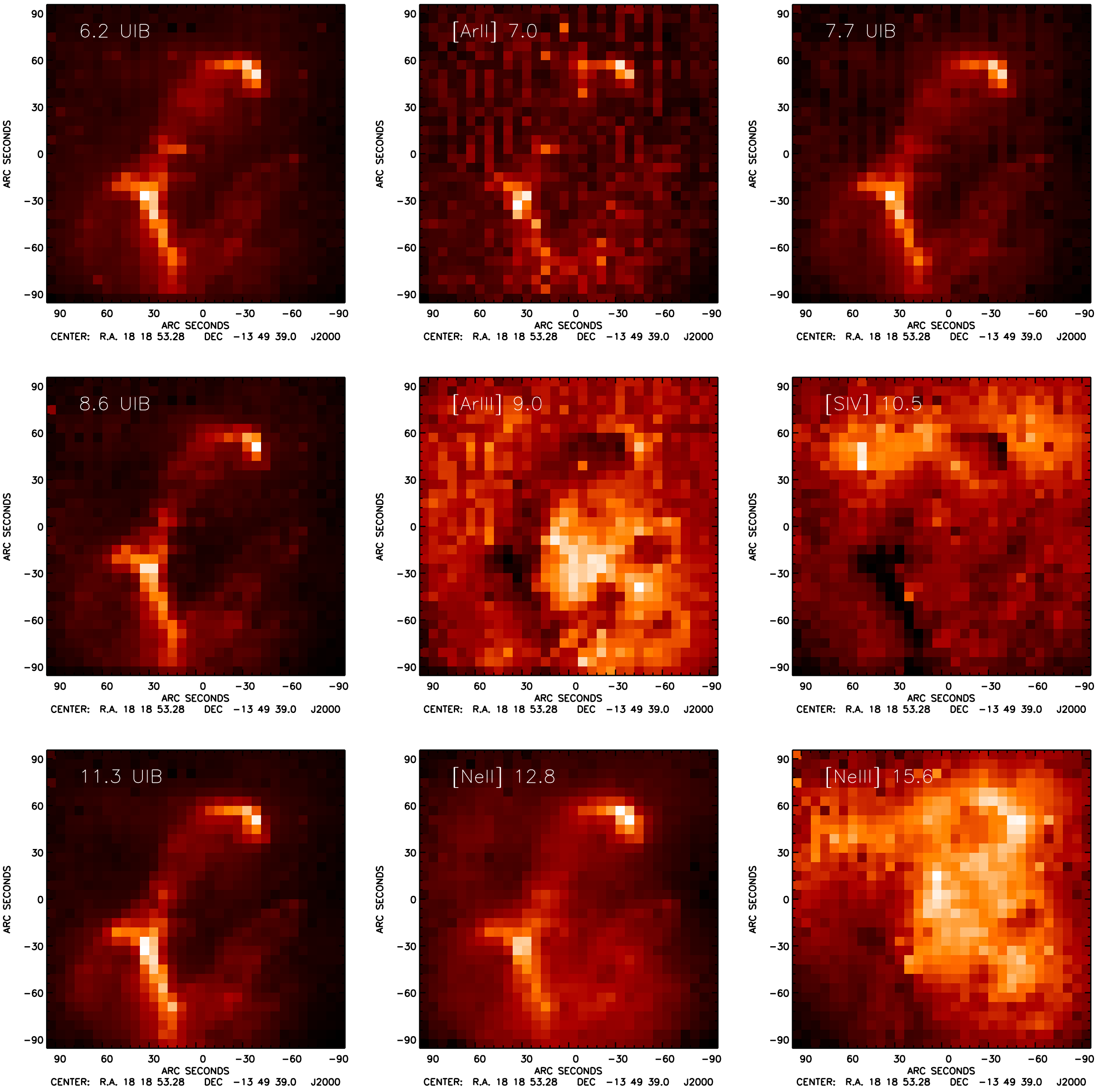

Fig. 5. Maps of the spatial brightness distribution of the decomposed ISOCAM-CVF spectra. The difference between the UIB and fine-structure lines can clearly be seen, with all of the UIB emission being confined to the pillar regions and the fine-structure lines being much more diffuse and located round the tips of Π_1 and Π_2 and the region between the two pillars.

emission feature to directly compare the spatial distribution of the UIBs to the emission in the ISOCAM broadband filters and observational data collected at other wavelengths.

The resulting image of the 7.7 μm UIB feature from the decomposition of the ISOCAM–CVF spectra is shown in Fig. 5. The emission clearly traces the structure of the first two columns Π_1 & Π_2, with the strongest emission observed on the head of Π_1 and on the ridge connecting the base of the first two pillars, no discrete sources are seen. The ISOCAM LW2 broadband filter image, taken from an observational dataset reported by Pi98 can be seen on the right of the 7.7 μm UIB feature. The LW2 broadband filter covered the wavelength region between 5–8.5 μm, giving an effective wavelength of 6.7 μm, and an effective resolution of 2.8″.

Comparing the two images presented in Fig. 6 it is easy to see similarities in the overall structure of the pillars, both displaying strong emission around the head of Π_1 and along the ridge connecting Π_1 and Π_2. The emission from these two regions is stronger by a factor of 3 than the head of Π_2. From the ISOCAM–CVF spectra it can be seen that the emission within the LW2 broadband region is dominated by contributions from three UIBs peaked at 6.2, 7.7 and 8.6 μm, with only a weak contribution from the underlying continuum (see Fig. 4), as also seen in ISOCAM spectroscopy of Orion B

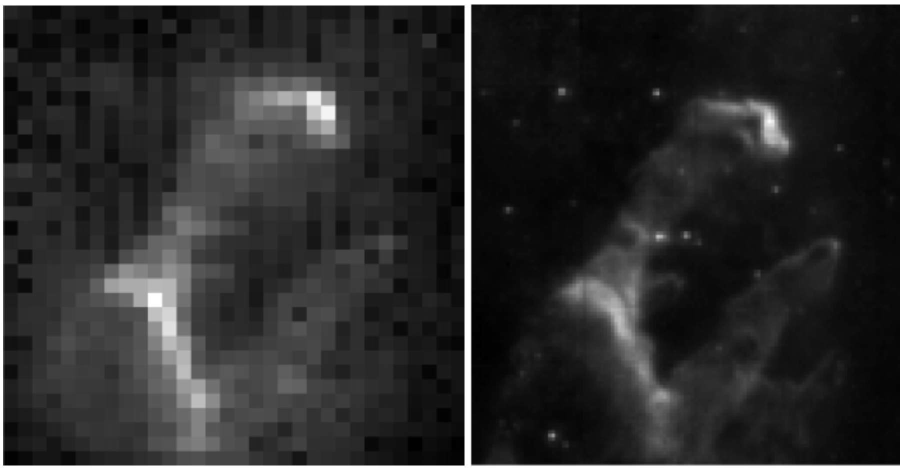

Fig. 6. *Left*: Image of the 7.7 μm UIB produced from the decomposition of the ISOCAM-CVF spectra. *Right*: The LW2 ISOCAM image of a $4' \times 4'$ FOV the pillar structures in M 16 taken from observations by Pilbratt et al. (1998; see paper for observation details).

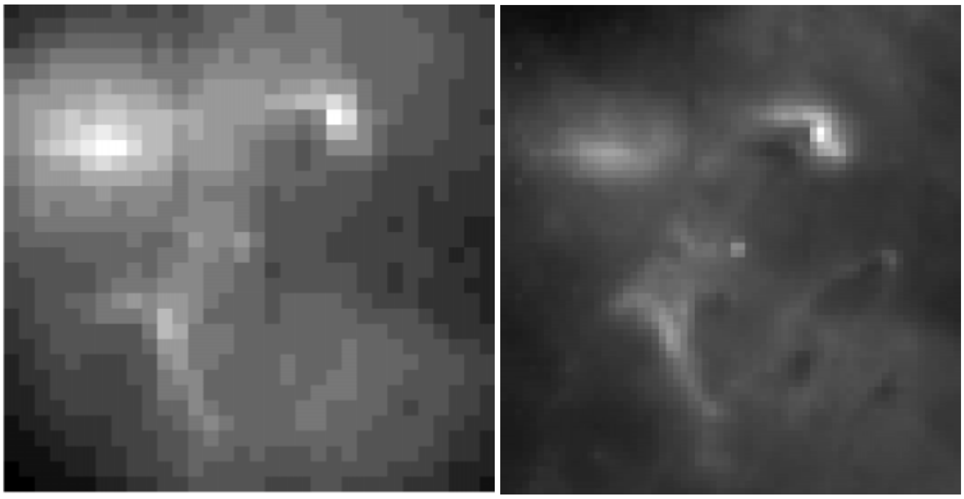

Fig. 7. *Left*: Image of the 13.5–15 μm continuum emission. *Right*: The LW3 ISOCAM image of a $4'.8 \times 4'.8$ field the pillar structures in M 16 taken from observations by Pilbratt et al. (1998; see paper for observation details). These two independent images confirm the reality of "Pilbratt's blob".

(Abergel et al. 2002). Therefore the vast majority of the emission seen in the LW2 image is emitted from the PDRs around the tip of Π_1 and the ridge below.

Comparisons of the LW3 broadband filter (12–18 μm) with the two spectral line images that fall within the wavelength region failed to fully account for all the features seen across the field. The [NeII] 12.8 μm emission correlates well with the emission from the pillar structures and the [NeIII] 15.6 μm diffuse emission seen throughout the field. However, neither spectral image shows any emission that would correlate with the bright region of emission seen to the northeast of Π_1, Pilbratt's blob, in the LW3 image or the broadband ISOCAM-CVF images presented in Fig. 2. We have produced an image of the continuum emission between the two Neon lines between 13.5–15 μm shown in Fig. 7 next to the LW3 image. There is clearly a great deal of correlation between the two images despite the difference in the angular resolution. This would suggest that the LW3 filter is dominated by the continuum as suggested by Abergel et al. (2002), even when strong emission from fine-structure lines are present within the wavelength range of the filter wheel.

We have found that the LW2 and the LW3 broadband filters are well correlated with the 7.7 μm UIB feature and the ~13.5–15 μm continuum, as previously reported by Abergel et al. (2002).

3.3. Photodissociation regions

The family of UIBs seen in our data have been widely observed by ISO in many astrophysical environments and has been extensively studied (Cohen et al. 1989; Allamandola et al. 1989). The spectral profiles in much of the published work are very similar, in both position and width, over a range of objects where the effective temperature and stellar radiation fields vary by a large range of magnitudes, $T_{\rm eff}$ = 11 000 to 50 000 K, and $G_0 \sim 1{-}10^4$ (Verstraete et al. 2001), where G_0 is the value of the FUV radiation field in units of the average interstellar radiation field (Habing 1968; Tielens & Hollenbach 1985).

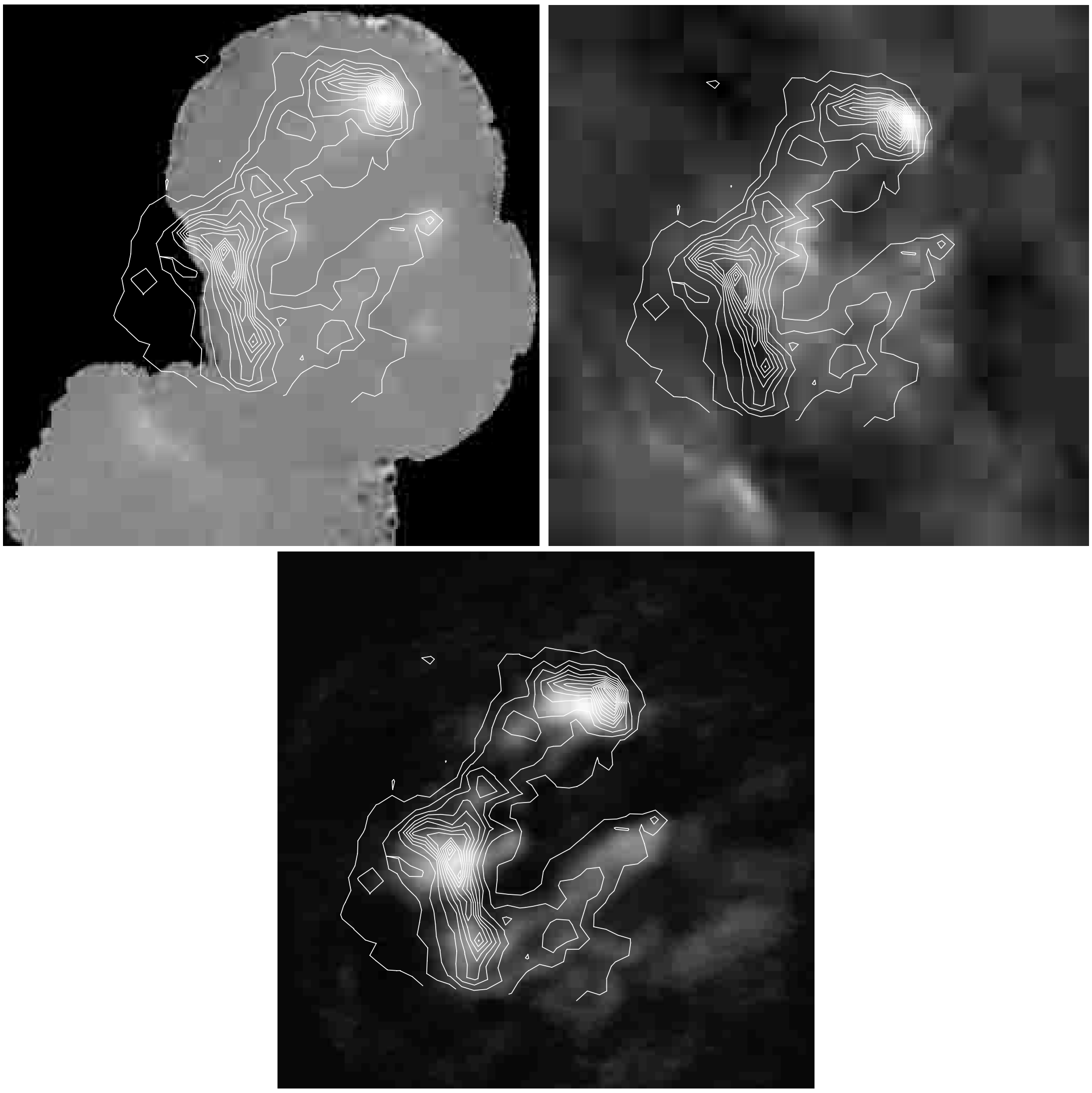

Fig. 8. *Upper left*: SCUBA 450 μm images of the pillar structures in M 16 overlaid with the contoured emission of the 7.7 μm PAH feature. *Upper right*: VLA image of M 16 again overlaid with UIB 7.7 μm emission. Expanded region of the VLA emission on the right. *Lower bottom*: ^{12}CO (J = 1−0) map (Pound, private communication) shows the distribution of molecular gas. (Contours levels are set at 10% of the peak emission beginning at 0.4 Jy.)

The UIB emission features has been widely attributed to C–C and C–H vibrational modes in Polycyclic Aromatic Hydrocarbons (PAHs) containing from 100–1000 C atoms (Lèger & Puget 1984; Allamandola et al. 1985; Joblin et al. 1995; Bo98) and have been demonstrated to be preferentially associated with regions of star formation (Laurent et al. 2000). The 8.6, 11.3 and 12.7 μm emission is believed to be associated with a C–H bond, and the remaining lines with C–C bonds. UIB emission originates in the interface between the molecular hydrogen and the HII region where the FUV radiation from massive stars dominates the heating and chemistry of the gas making them a good tracer for PDRs (Rathborne et al. 2002).

Luminous PDRs are also good pointers to newly formed young massive stars, but are also interesting themselves as possible sites for triggered low mass star formation and contain all of the atomic gas and ~90% of the molecular gas in the Galaxy (Hollenbach & Tielens 1999). PDRs are also responsible for the production of most of the Mid-IR radiation (MIR) observed in the Interstellar Medium (ISM).

Comparisons between the 7.7 μm UIB emission map and images obtained at 450 μm using SCUBA, free-free radio emission at 8.69 GHz using NRAO Very Large Array (VLA) and ^{12}CO (J = 1−0) maps of Pound (private communication) are presented in Fig. 8. Full details of observations and data reduction for both 450 μm and VLA images are described in Wh99. Cold dust ($T \sim 10$ K) is assumed to be the source of the 450 μm SCUBA emission and is associated with regions of high HI column density, the free-free radio emission traces the ionised gas and the ^{12}CO (J = 1−0) traces the molecular gas.

Three compact emission regions can be seen in the SCUBA image (upper left panel Fig. 8), relating to dense cores at the heads of the pillars. There is good correlation between the emission seen in the SCUBA image, located at the tip of Π_1 and weaker extended emission along the ridge with the peak of the 7.7 μm UIB emission located between the the ionising source and the SCUBA emission. From this we conclude that the UIB emission peaks appears to be located at the front edge of the molecular gas where the ionised gas flow starts, consistent with hot grains directly exposed to the FUV field.

The free-free radio emission (see upper right panel Fig. 8) traces the ionised gas emitted from the front and rear surfaces of the pillars providing a complete picture of the distribution of ionised gas around the pillars. The radio emission is more difficult to interpret, but a bright region of emission is clearly visible wrapping around the tip of Π_1, which peaks just in front (with respect to the ionising source) and a weaker extended region is seen lying in front of the bright ridge seen in the 7.7 μm UIB emission. The ^{12}CO (J = 1−0) emission (see lower bottom panel Fig. 8) shows two molecular core that correlate with emission seen in the UIB map, at the head of Π_1 and the second peaking on the ridge at the base of Π_1.

The emission from all three images is consistent with the presence of a PDR on the tip of Π_1 between the cold molecular core and HII region. The 7.7 μm UIB emission from the ridge suggests the presence of a PDR, the radio emission in front of the ridge and presence of the dense concentration of molecular material seen in the ^{12}CO (J = 1−0) located near the base of Π_1 is consistent with this. The lack of any emission from the other two columns would suggest either, that no PDRs are present, or that the geometry is such that the emission from any PDRs are hidden from our line-of-sight. Wh99 reported limb-brightening of Π_2 in the radio images, possibly indicating the presence of a PDR on the hidden side of Π_2. This would support the assumption that the ionising source lies in a plane between the Π_1 and Π_2 & Π_3 as previously discussed.

3.4. Modelling the fine-structure lines

Fine-structure line ratios of different ionisation states of the same elements, such as [ArIII] 9.0 μm/[ArII] 7.0 μm and [NeIII] 15.6 μm/[NeII] 12.8 μm, are very sensitive to the spectral shape of the incident FUV radiation field and independent of their abundances. Through comparison of the ratios of the integrated fluxes of the four fine-structure lines and theoretical values produced by models we are able to determine the properties of the ionising radiation field.

We have concentrated our effort on the [NeIII] 15.6 μm/[NeII] 12.8 μm line ratio since the [NeII] 12.8 μm and [NeIII] 15.6 μm lines span the widest range of ionisation potential, 21.6 and 41.1 eV respectively, compared to other possible line ratios in the CVF wavelength region, i.e. [ArII] 7.0 μm and [ArIII] 9.0 μm is 15.8 and 27.6 eV, respectively. Therefore the Neon ratio offers the greatest sensitivity to the incident FUV radiation field. Additionally the wavelength of the two Neon lines are relatively close to one-another allowing differential extinction effects to be neglected (~1%). Moreover, the calibration uncertainties in the observed fluxes are minimised by taking the ratio of two lines, from approximately 30% to 10% (Schaeidt et al. 1996). The emission of the two Neon lines has been to produce a ratio map, presented in Fig. 9. From this ratio map we can see how the ratio, and therefore the properties of the FUV radiation field, change across the field.

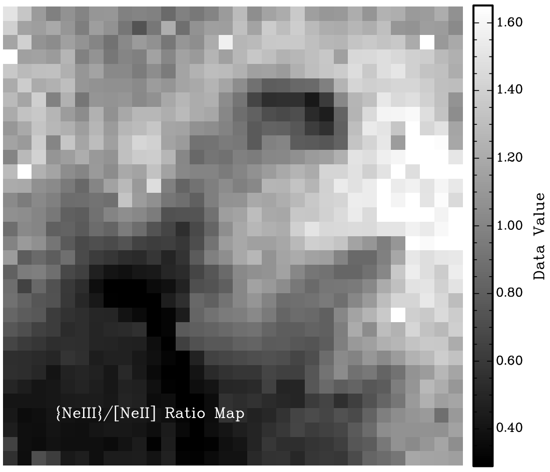

Fig. 9. Ratio maps of [NeIII] 15.6 μm/[NeII] 12.8 μm. The pillars can be seen silhouetted against the bright HII region. The colour bar to the right of the map displays the ratio value across the field, ranging from 0.4 (black) to 1.6 (white).

Using the photoionisation code CLOUDY (version 94.01, Ferland 1993) we have calculated the theoretical fine-structure line ratios of [NeIII] 15.6 μm/[NeII] 12.8 μm for different values of the total surface ionising flux, Φ (photons cm^{-2} s^{-1}), and a range of hydrogen density to produce the data presented in Fig. 10. A Kurucz stellar atmosphere model with a temperature of 47 000 K has been used to reproduce the continuum generated by the O5 and O5.5 stars suggested by Pound (1998) to be responsible for most of the ionising radiation impinging onto the surface of the pillars. We have assumed typical HII abundances (cf. Hazy, Ferland 1996). A comparison of these theoretical values with values estimated from the ratio maps should allow us to determine the strength of the FUV radiation field around the tips of the pillars and on the dense core at their heads.

The high ratio regions are found almost exclusively around the tips of the three pillars with values ranging between 1.3–1.6. Taking an average from a 16 pixel area in front of Π_1 centred at RA = $18^{\mathrm{h}}18^{\mathrm{m}}8\overset{\mathrm{s}}{.}90$, Dec = $-13°48'30\overset{''}{.}15$ (J2000) a value of ~1.52 was obtained for the neon ratio. Assumimg an upper limit for the hydrogen particle density in the HII region of 1×10^3 cm^{-3} an estimate of the upper limit for Φ can be calculated. Taking into account the errors due to the calibration uncertainties we calculate an upper level for Φ to be between $2{-}3 \times 10^{10}$ photons cm^{-2} s^{-1}, but if we assume a more reasonable estimate for the hydrogen density of ~500 (electron density around the tip of Π_1 report by WH99 from VLA observations) a value of Φ in the region of $\sim 1 \times 10^{10}$ photons cm^{-2} s^{-1} is obtained. These values are in excellent agreement with the values reported by Wh99 from the VLA observations of the ionised gas around the tip of the pillars.

Using these resulting values for the ionising photon flux the total ionising flux emitted by the stars in NGC 6611 can be calculated, found to be $\sim 2 \times 10^{49}$ photons s^{-1}, in good agreement with the value of 3.7×10^{49} photons s^{-1} calculated by

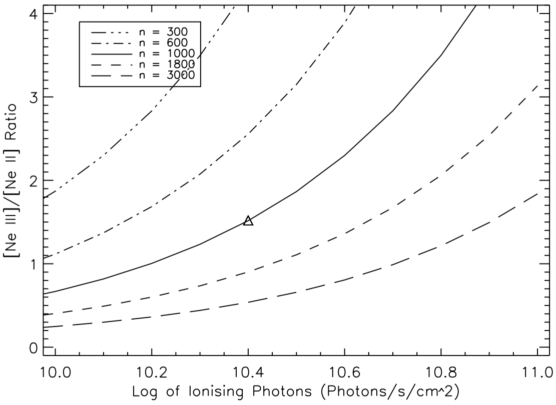

Fig. 10. Results obtained from CLOUDY for the [NeIII]/[NeII] ratio for different values of ionising photons on the surface of the pillars and the hydrogen density, *n* (H_2 cm^3). The ratio obtained from the decomposition of the CVF data is represented by a triangle.

Allen et al. (1999) from Br_γ emission observed from the surface of Π_2. This value is a factor of ten smaller than theoretical values presented by He96 and six times smaller than the theoretical values presented by Pound, $\sim 2 \times 10^{50}$ and $\sim 1.2 \times 10^{50}$ photons s^{-1}, respectively. There are several possible explanations for the discrepency between the value obtained from our data and the theoretical value calculated from stellar models. First, the effects of attenuation of the photon flux due to absorption by dust grains and any reionisation taking place between the ionising stars and the tips of the pillars has not been considered. In a recent study of a similar photoionised region in the Trifid nebula, bright-rimmed globule TC2, (Lefloch et al. 2002) the impinging photon flux calculated was found to be a factor of between 5–6 smaller than the theoretical photon flux derived from the Lyman continuum luminosity of the ionising star located a projected distance of 1 pc. This is fully consistent with our results. Second, it has been assumed that the ionising stars and the pillars are in the same plane in the sky. This is not necessarily true, in which case the geometry will result in a lower photon flux impinging onto the pillars and therefore a reduction in the observed photon flux.

Taking these explanations into account we believe our results our consistent with the hypothesis that the pillars are being photoionised by a group of O5–O5.5 stars located a projected distance of ∼2 pc to the north-west.

4. Conclusions

The main conclusions based on the ISOCAM-CVF data presented in the previous sections can be summarised as follows:

1. We have presented MIR maps of the brightness distribution of emission features over the field of M 16 produced from the decomposition of low resolution spectra obtain using ISOCAM-CVF. We have compared these maps with LW2 (5–8.5 μm) and LW3 (12–18 μm) images reported by Pi98 and found that the LW2 filter is dominated by UIB emission and the LW3 filter is dominated by continuum emission despite the presence of strong emission from [NeII] 12.8 μm and [NeIII] 15.6 μm, as previously reported by Abergel et al. (2002).
2. All of the UIB emission is contained within the pillars of M 16 with the vast majority being emitted from an the area around the tip of Π_1 and the ridge connecting the Π_1 & Π_2 to the parental molecular cloud. The bright area around the tip of Π_1 is situated in between the cold dust distribution traced by SCUBA 450 μm maps and a region of hot ionised gas traced by the VLA map, where we would expect a PDR to be located.
3. The lack of any UIB emission from Π_2 and Π_3 could be the due to several factors, a combination of weak emission from the pillars, the poor angular resolution of the instrument or the geometry, i.e. if the ionising stars lie in a plane between Π_1, and Π_2 the PDRs produced on Π_2 and Π_3 cloud would be out of our line-of-sight. This conclusion is supported by the limb-brightening reported by Wh99.
4. Our analysis of the CVF data has failed to reveal any information concerning the origin of the emission referred to as Pilbratt's blob. The CVF spectrum presented in Fig. 2 shows some evidence that the Pilbratt's blob has some weak spectral line emission on top of a steep continuum. The decomposition of the data into maps of the spectral features, i.e. [NeII] 12.8 μm and [NeIII] 15.6 μm the two main features within the LW3 broadband filter, failed to produce any correlation with Pilbratt's blob, but an integrated image produced using the CVF data over a similar wavelength region (13.5–15 μm; see Fig. 7) did correlate well with the LW3 image. From this we conclude that the emission seen towards Pilbratt's blob is continuum emission due to VSGs warmed by a presently unknown source.
5. Using the photoionisation code CLOUDY, Kurucz stellar atmosphere model (47 000 K) and the results of the decomposition of the CVF data, the effective ionising flux impinging onto the tips of the pillars has been calculated to be $\sim 1\text{–}3 \times 10^{10}$ photons cm^{-2} s^{-1}, in agreement with the VLA observations reported by Wh99.

Acknowledgements. We gratefully acknowledge Marc Pound for providing the ^{12}CO ($J = 1\text{–}0$) maps, Mike Burton, Larry Morgan and Mark Thompson for some helpful discussions and advice. We also thank an anonymous referee for some useful comments and suggestions. The ISOCAM data presented here have been analysed using the CIA, a joint development by ESA Astrophysics Division and the ISOCAM Consortium led by the ISOCAM PI, C. Cesarsky, Direction General of ESO. The NOT image was based on observations made with the Nordic Optical Telescope, operated on the island of La Palma jointly by Denmark, Finland, Iceland, Norway, and Sweden, in the Spanish Observatorio del Roque de los Muchachos of the Instituto de Astrofisica de Canarias. The James Clerk Maxwell Telescope is operated on behalf of the Particle Physics and Astronomy Research Council of the UK, The Netherlands Organisation for Scientific Research and the National Research Council of Canada.

References

Abergel, A., Bernard, J. P., Boulanger, F., et al. 1996, A&A, 315, L329
Abergel, A., Bernard, J. P., Boulanger, F., et al. 2002, A&A, 389, 239
Allamandola, L. J., Tielens, A. G. G. M., & Barker, J. R. 1985, ApJ, 290, L25

Allamandola, L. J., Tielens, A. G. G. M., & Barker J. R. 1989, ApJ, 71, 733

Allen, L. E., Burton, M. G., Ryder, S. D., Ashley, M. C. B., & Storey, J. W. V. 1999, MNRAS, 304, 98

Bertoldi, F. 1989, ApJ, 346, 735

Boulanger, F., Boisssel, P., Cesarsky, D., & Ryter, C. 1998, A&A, 339, 194 (Bo98)

Cesarsky, C. J., Abergel, A., Agnese, P., et al. 1996, A&A, 315, L32

Cohen, M., & Kevin, V. 1989, AJ, 98, 1563

Desert, F.-X., Boulanger, F., & Puget, J. L. 1990, A&A, 237, 215

Ferland, G. J. 1993, University of Kentucky, Dept. of Physics & Astronomy Internal Report

Ferland, G. J. 1996, Hazy, a Brief Introduction to CLOUDY 90, University of Kentucky, Dept. of Physics & Astronomy Internal Report

Fukuda, N., Hanawa, T., & Sugitani, K. 2002, AJ, 568, L127 (FSH02)

Habing, H. J. 1968, Bulletin, Astr. Inst. Netherlands, 19, 421

Hester, J. 1991, PASP, 103, 853

Hester, J., Scowen, P. A., Sankrit, R., et al. 1996, AJ, 111, 2349 (He96)

Hillenbrand, L. A., Massey, P., Strom, S. E., & Merrill, K. M. 1993, AJ, 106, 1906 (Hi93)

Hollenbach, D. J., & Tielens, A. G. G. M. 1999, Rev. Mod. Phys., 71, 173

Joblin, C., Boissel, P., Lèger, A., d'Hendecourt, L., & Dèfournean, D. 1995, A&A, 299, 835

Kessler, M. F., Steinz, J. A., Anderegg, M. E., et al. 1996, A&A, 315, L27

Laurent, O., Mirabel, I. F., Charmandaris, V., et al. 2000, A&A, 359, L887

Le Floc'h, E., Mirabel, I. F., Laurent, O., et al. 2001, A&A, 367, 487

Lefloch, B., & Lazareff, B. 1994, A&A, 289, 559

Lefloch, B., Cernicharo, J., Rodríguez, L. F., et al. 2002, ApJ, 581, 335

Lèger, A., & Puget, J. L. 1984, A&A, 137, L5

McCaughrean, M. 1997, Herbig-Haro Flows and the Birth of Stars, IAU Symp., 182, 551

McCaughrean, M. J., & Andersen, M. 2002, A&A, 389, 518

Moutou, C., Vertraete, L., Lèger, A., Sellgren, K., & Schmidt, W. 2000, A&A, 354, L17

Onaka, T. 2000, The Institute of Space and Astronautical Science Report SP No. 14

Ott, S., Abergel, A., Altieri, B., et al. 1997, Astronomical Data Analysis Software and Systems VI, ASP Conf. Ser., 125

Pilbratt, G. L., Altieri, B., Blommaert, J. A. D. L., et al. 1998, A&A, 333, L9 (Pi98)

Pound, M. W. 1998, ApJ, 493, L113

Rathborne, J. M., Burton, M. G., Brooks, K. J., et al. 2002, MNRAS, 331, 85

Schaeidt, S. G., Morris, P. W., Salama, A., et al. 1996, A&A, 315, L55

Starck, J. L., Aussel, H., Elbaz, D., Fadda, D., & Cesarsky, C. 1999, A&AS, 138, 365

Sugitani, K., Tamura, M., Nakajima, Y., et al. 2002, A&A, 342, 233

Tielen, A. G. G. M., & Hollenbach, D. 1985, ApJ, 291, 722

Thompson, R. I., Smith, B. A., & Hester, J. J. 2002, ApJ, 570, 749

Verstraete, L., Puget, J. L., Falgarone, E., et al. 1996, A&A, 315, L337

Verstraete, L., Pech C., Moutou, C., et al. 2001, A&A, 372, 981

White, G. J., Nelson, R. P., Holland, W. S., et al. 1999, A&A, 342, 233 (Wh99)